A microstructure sensitive model for deformation of Ti-6Al-4V describing Cast-and-Wrought and Additive Manufacturing morphologies

M.A. Galindo-Fernández [a], K. Mumtaz [a], P.E.J. Rivera-Díaz-del-Castillo [b], E.I. Galindo-Nava [c], H. Ghadbeigi [a,*]

[a] Department of Mechanical Engineering, The University of Sheffield, Mappin Street, Sheffield S1 3JD, UK
[b] Engineering Department, Lancaster University, Engineering Building, Lancaster LA1 4YW, UK
[c] Department of Materials Science and Metallurgy, University of Cambridge, 27 Charles Babbage Rd, Cambridge CB3 0FS, UK

HIGHLIGHTS

- A new physically-based model has been developed to describe strength and flow stress of AM and Cast-and-wrought build Ti-64 alloys.
- Microstructural evolution due the thermal exposure should be considered in the model for more accurate prediction at higher temperatures.
- The proposed model could be used to design new alloys with specific mechanical properties using bespoke microstructural properties.

GRAPHICAL ABSTRACT
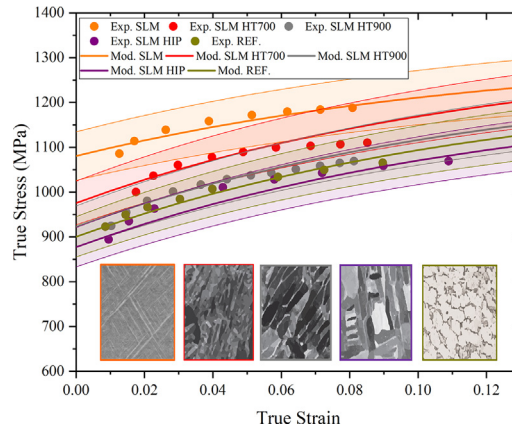
ARTICLE INFO

ABSTRACT

Microstructural variations affect deformation response of materials and it is not presented in most of plastic flow prediction models. This work presents a unified description for the deformation response of Ti-6Al-4V (Ti-64) that successfully captures the differences in strength between microstructures produced by conventional cast & wrought routes (C&W) and those obtained by Additive Manufacturing (AM), under various deformation conditions. In the developed model the grain morphology, grain size, phase volume fractions and phase chemical compositions have been linked to the mechanical properties of the studied Ti-64 alloys to predict the effect of processing routes on deformation behaviour of the materials. The model performance has been tested on seven different microstructures from C&W to AM processing routs. It has been found that altering the microstructure greatly affects the yield strength of the tested materials. Additionally, the strength of Ti-64 was found to be mostly affected by the relative volume fraction of α, β and α', and their respective morphology. The results showed that the model not only successfully predicts the strength of martensitic structures generated through AM but also those obtained by quenching in conventional C&W processing. The findings from this study also suggest that the model could be extended to other titanium alloys within the $\alpha + \beta$ family.

* Corresponding author.
  E-mail address: h.ghadbeigi@sheffield.ac.uk (H. Ghadbeigi).

Nomenclature

α_p	alpha globular phase
α_s	secondary alpha phase
σ_Y	yield strength
α'	martensite
k_{HP}	Hall-Petch coefficient
D_α	mean grain size of α phase
W_α	α phase width's lath
σ_0	friction stress
$V_{\alpha s}$	volume fraction of secondary α phase
$D_{\alpha s}$	secondary α grain size
σ_α	friction stress in α
V_α	volume fraction of α phase
σ_β	friction stress in in β
V_β	volume fraction of β phase
σ_{prism}^α	stress required activating prismatic slip
G	activation energy
T	temperature
$\dot{\varepsilon}$	strain rate
η	material's constant
κ	material's constant
μ	shear modulus
k_B	Boltzmann constant
σ	flow stress
M	Taylor's factor
b	Burgers vector
ρ	average dislocation density
k_1	dislocation generation coefficient
f	recovery coefficient
ρ_0	initial dislocation density
ε_{trans}	transformation strain
$\rho_{\alpha'}$	initial dislocation density in a single martensite lath
$d_{\alpha'}$	mean lamellar spacing
$W_{\alpha'}$	martensitic lamellar thickness
E	Young's modulus
$\rho_{0\alpha'}$	martensitic initial dislocation density

1. Introduction

Titanium alloys have outstanding properties such as corrosion resistance, high strength-to-weight ratio even at high temperatures, that makes them a suitable candidate for high demanding applications such as the ones in aerospace industry [1,2]. Among the Ti-alloy families, Ti-6Al-4V (Ti-64) has been widely used in developing technologies such as Additive Manufacturing (AM) [3–5] as well as traditional processing routes including cast and wrought (C&W) operations [6,7]. AM is an emerging technology that can be used to fabricate titanium alloys with complex geometrical features and reduce material waste, production time and costs. Moreover, current AM research focuses on developing the manufacturing processes using well-established wrought alloys through pre-alloyed powders, nonetheless large differences in the microstructure and mechanical properties have been pointed between wrought and AM materials [6,8].

Due to the importance of Ti-64 alloy, modelling its mechanical properties has been a relevant topic for materials scientists and engineers [9]. In this context, constitutive equations are highly used to describe flow stress of materials during plastic deformation and are commonly implemented into Finite Element (FE) techniques to simulate manufacturing processes such as forming and metal cutting [10–12]. There are different models available to predict the flow stress of Ti-64 alloys where macro scale uniaxial testes are used to determine/verify material's constants

[2]. Empirical models [13–16] are a mathematical representation of experimental data and usually describe flow stress as a function of strain, strain rate and temperature, while the physically based models link physical phenomena with macroscopic mechanical behaviour [9,17–20]. The most recent approach is the Artificial Intelligence Techniques (AIT) such as Artificial Neural Network (ANN) [11,21,22] and Fuzzy Neural Network (FNN) [23].

Empirical models such as the Johnson-Cook (JC) model [13] and its variations [14] and Khan-Huang-Liang (KHL) and modified KHL models [15,16] have been widely used due to small number of parameters required to calibrate the models for a given material. Their major drawback is the lack of clarity on the different mechanisms occurring during plastic deformation, instead the material constants are fitted for specific experimental data. Consequently, the set of parameters is unique for a given material with a specific processing history, therefore large variations in the resulted microstructures are expected changing their mechanical properties, this is evident due to the extensive list of JC material's constants reported for Ti-64 [14,24–27].

Early physically based models were proposed based on evolution of the dislocation density such as Kocks-Mecking [17,28]. Bergström and Roberts [18] proposed a variation of Kocks-Mecking formulation to incorporate more complex mechanisms such as partitioning dislocation density into mobile and immobile dislocations. More recent studies have proposed flow stress models for Ti-64 based on the activation energy required to generate plastic deformation [9,19]. However, the high number of material constants to be validated is the biggest challenge in using this approach limiting their implementation into FE techniques [12]. In addition, hybrid modelling combining numerical modelling (FE) and mathematical modelling have been proposed to quantify the effect of microstructural features within the strength and flow stress of materials [29,30].

Artificial Intelligence Techniques (AIT) use machine learning algorithms to predict mechanical properties during different processing histories. However, these techniques are used to predict tensile strength, yield strength and elongation to failure rather than the flow stress of materials [22,23]. The AIT based models can accurately predict the mechanical properties of any material when the processing parameters (e.g. deformation temperature, strain and strain rate) are well defined. However, these are computationally and experimentally expensive requiring many experimental results to train the models and cannot quantify different phenomena occurring during plastic deformation [31].

All the developed models have been focused on conventional manufacturing processes and agree that the mechanical properties of Ti-64 are highly affected by its microstructure, which is dependent on the processing history. Moreover, due to recent development of AM techniques, prediction of mechanical properties of additively manufactured Ti-64 is becoming critically important [31]. To the best knowledge of the authors, no constitutive model is available for Ti-64 manufactured under a wide range of processing routes (Cast &Wrought and AM).

The aim of this study is to present a new physically based model capable of describing the deformation response of additively manufactured Ti-64 and contribute to the current knowledge in cast wrought (C&W) technology. The new proposed model will be used to predict deformation behaviour, irrespective of the processing route, via linking relevant microstructural features with the strengthening mechanisms; the former covers grain morphology, grain size, volume fraction and chemical composition for a wide range of deformation conditions (temperature and strain rate effects). Therefore, this study makes a major contribution to the understanding of processing routes in Ti-64 and could be used for designing future Ti-AM alloys.

2. Titanium and the effect of processing routes

Ti-64 is part of the $\alpha + \beta$ family, depending on the hot working route, three commercial microstructures are available namely, lamellar,
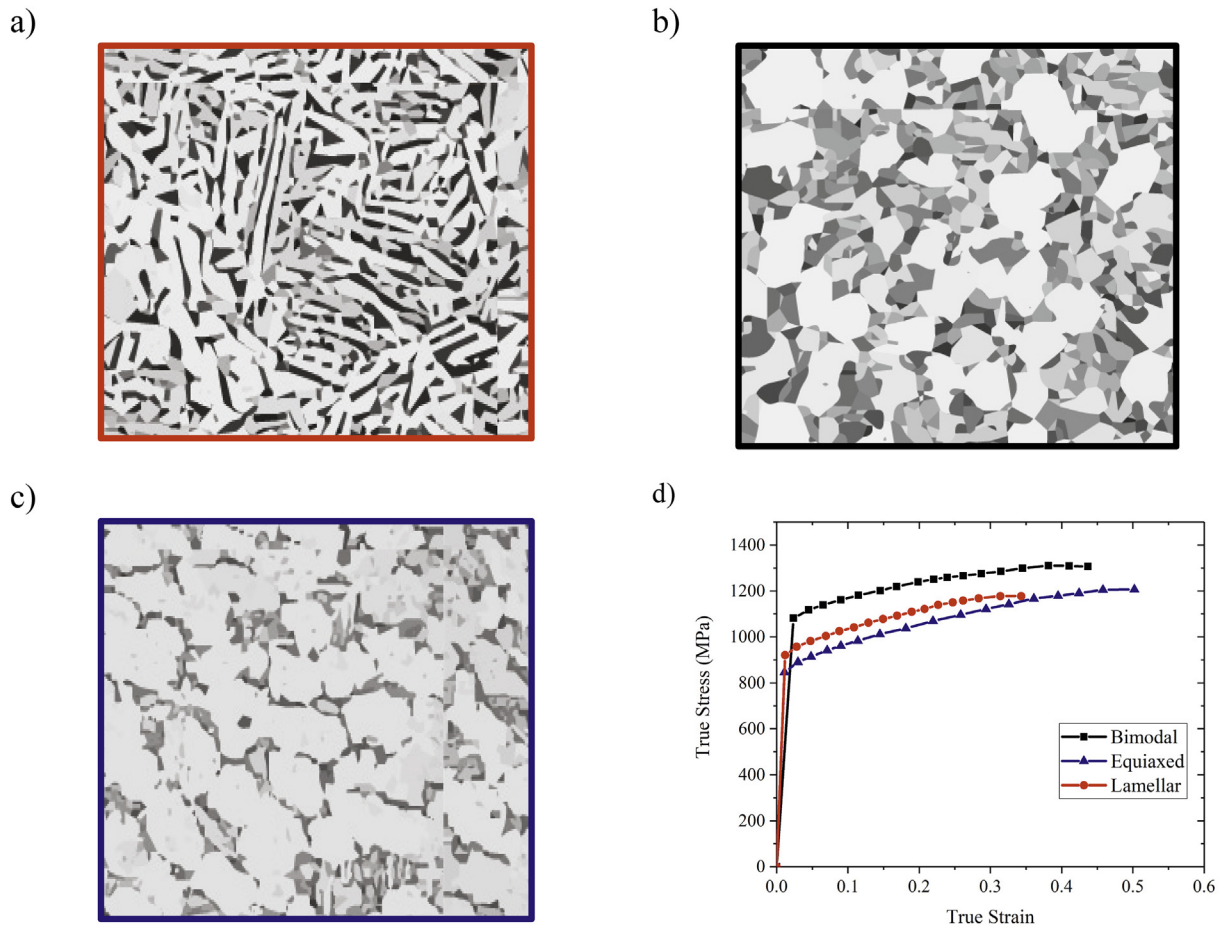
a)

b)

c)

d)

Fig. 1. Typical wrought Ti-64 microstructures: (a) lamellar (b) bimodal (c) equiaxed and (d) their representative mechanical response, at room temperature and a strain rate of $10^{-3}\,\mathrm{s}^{-1}$ as reported in [32].

bimodal and equiaxed. Therefore Ti-64 present diverse mechanical properties. Fig. 1 shows schematics of Ti-64 microstructures and the effect of microstructures on the corresponding mechanical response. Despite large variations observed in the microstructural features, these are formed by α and β constitutive phases. Fully lamellar structures are formed by lamellas of α and β phases distributed as a repeating pattern (Fig. 1.a), bimodal structures (Fig. 1.b) are formed by the combination of two morphologies; globular structures (α_p), secondary alpha (α_s) and β phase. Equiaxed structures are formed by primary equiaxed α_p grains (Fig. 1.c).

The presented microstructures in Fig. 1 have been studied extensively in a wide range of deformation conditions [7,9,16,32–34], however with the introduction and rapid development of AM technologies, specifically powder bed assisted techniques such as Selective Laser Melting (SLM), Powder Laser-Deposition (PLD) and Electron Beam Melting (EBM), new microstructures are currently achieved [4,35,36].

The microstructures shown in Fig. 1 are formed through phase transformation of the β phase to α phase occurring by diffusion-controlled nucleation and growth during hot deformation [37], whereas in SLM and PLD technologies the martensitic transformation occurs by the inherent fast heating and cooling cycles of the printing process [35,38]. A typical SLM build microstructure is shown in Fig. 2 where in the produced martensite has a hexagonal-closed packed structure and it is designated as α' [39].

Fig. 3 shows the comparison of mechanical response of Ti-64 hot worked and AM martensitic structures during tensile tests reported in the literature. According to obtained stress-strain curves, the yield and tensile strength of the SLM build parts (green area) are higher compared

to wrought material (red area). This, however, is achieved at the expense of reduced ductility in the former. Moreover, the ductility of the SLM build microstructure show no apparent improvement even after heat treatments, where the strength of the material reduces considerably (the blue section in Fig. 3).

This can be explained by the lack of either α or β phases in SLM components, as a result α' provides higher strength to the material [3,40].
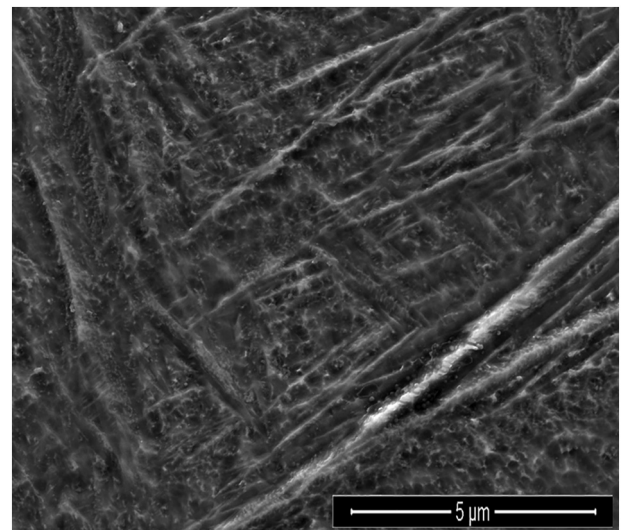
Fig. 2. Typical Ti-64 martensitic structure achieved by Selective Laser Melting.
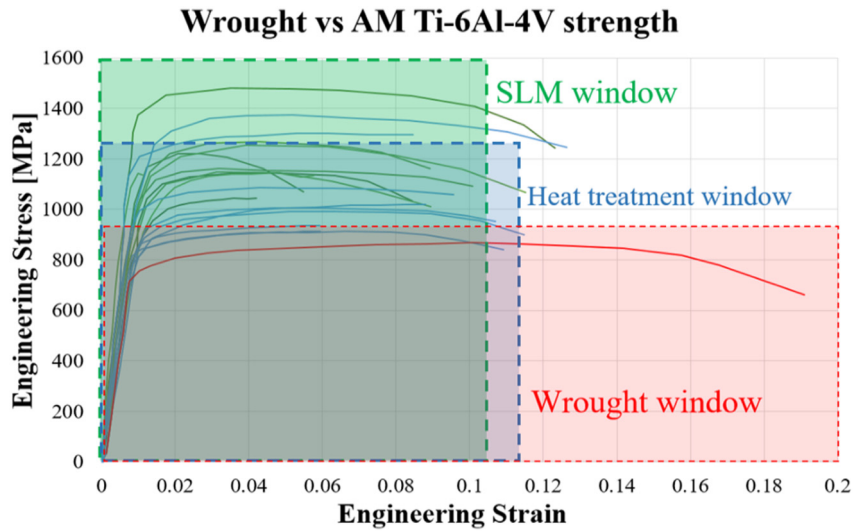
Wrought vs AM Ti-6Al-4V strength

Fig. 3. Tensile tests comparison of hot worked, SLM, heat treated SLM produced components of Ti-6Al-4V. As reported in [4,35,36,39,43–47].

Additionally, residual stresses can be present [4], therefore, a higher dislocation density is expected in AM built components [31,41]. Grain boundary hardening can also significantly affect the mechanical properties of these microstructures as small laths of less than a micrometre are observed in SLM and PLD components [39,42], while C&W present typical grain sizes in the range of 3–15 μm [36,38,43,44].

3. Model development

A physically based model has been developed to quantify the strength of Ti-64 followed by the prediction of flow stress in relation to the average dislocation density evolution due to plastic deformation. It is assumed that there are three main strengthening mechanisms to take place, including grain boundary strengthening, solid solution relative to volume fraction of $\alpha + \beta$, and forest hardening.

3.1. Yield strength prediction

The Hall-Petch relationship [48] was used to describe the yield strength (σ_Y) in order to capture the effect of microstructural morphologies. Given the fact that C&W Ti-64 commercial morphologies contain well defined α phase, for this work, only this phase was considered in the grain boundary strengthening mechanism:

$$\sigma_Y = \sigma_0 + \frac{k_{HP}}{\sqrt{D_\alpha}} \tag{1}$$

where D_α is the mean grain size of α phase (in microns), k_{HP} is the Hall-Petch coefficient of a given material and σ_0 is the friction stress that is the critical resolved shear stress to initiate slip in a grain. Eq. (1) is used for equiaxed structures whereas lamellar structures possess a typical lath shape; therefore, the width of each lath (W_α) is taken into account (i.e. the thinner side of the lath). For a bimodal microstructure, the second term in Eq. (1) will be substituted by a rule of mixture that takes into account primary α phase (D_α), secondary alpha grain size ($D_{\alpha s}$) and the relative volume fraction of secondary alpha phase ($V_{\alpha s}$);

$$\sigma_Y = \sigma_0 + k_{HP}\left(\frac{V_{\alpha s}}{\sqrt{D_\alpha}} + \frac{1-V_{\alpha s}}{\sqrt{D_{\alpha s}}}\right) \tag{2}$$

The friction stress (σ_0) includes the contributions of α and β phases into the strengthening mechanisms and for this study, it is assumed to

be affected mainly by solid solution effects [49]. The friction stress has been considered for both relative phase fractions as it is shown in Eq. (3) where solid solution strengthening effect of individual phases (σ_α in α and σ_β in β phases) and the volume fraction of α (V_α) has been considered:

$$\sigma_0 = \sigma_\alpha V_\alpha + \sigma_\beta(1-V_\alpha) \tag{3}$$

The friction stress in α includes a stress term, σ_{prism}^α, required to activate prismatic slip that is the main slip mode in α-Ti, as well a solid solution strengthening term in α, σ_{ss}^α. The critical prismatic slip stress σ_{prism}^α of 90 MPa was reported for prismatic slip in α-Ti single crystals [50] by measuring the critical resolved shear stress. The solid solution strengthening term in α is calculated using the equation, Eq. (4), derived by Labusch [51]:

$$\sigma_{ss}^\alpha = \left(\sum_i B_i^{3/2} x_i\right)^{2/3} \tag{4}$$

where x_i is the atomic concentration of element i in α and B_i is a strengthening constant related to the local size and modulus distortions of element i in α-Ti [52] given by:

$$B_i = \lambda\mu\left(\eta_i' + 16\delta_i\right)^{3/2} \tag{5}$$

where λ is a constant that depends on the base alloy and;

$$\eta_i' = \frac{|\eta_i|}{1 + 0.5\eta_i} \tag{6}$$

$$\eta_i = \frac{\mu_i - \mu_{Ti}}{\mu_{Ti}} \tag{7}$$

$$\delta_i = \frac{r_i - r_{Ti}}{r_{Ti}} \tag{8}$$

Eqs. (6) and (7) are the modulus differences and Eq. (8) lattice strain of element i in Ti, and μ_i and r_i are the shear modulus and atomic radius of element i, respectively. The values of μ_i and r_i for Ti, Al and V were obtained from [53] and λ was determined for Ti using experimental data of binary Ti-Al and Ti-Zr alloys through fitting Eq. (4) to the resolved stress increasing with composition [49,54]. Table 1 shows the parameters obtained for α phase in Ti-64.

Table 1
Parameters used for solid solution strengthening contributors.

Parameter	Dimension	Value	Reference
λ	Dimensionless	0.0082	Fitted
B_{Al}	MPa/at$^{2/3}$	1813	Calculated
B_V	MPa/at$^{2/3}$	127	Calculated
Al concentration in α	Dimensionless	0.125	[33]
V concentration in α	Dimensionless	0.018	[33]

Combining the values presented in Table 1 and Eq. (4), the solution strengthening contribution in α can be calculated as $\sigma_{ss}^{\alpha} = 454$ MPa. This gives the friction stress to be equal to $\sigma_{\alpha} = 544$ MPa. As for the friction stress of β, there are very few studies reporting solid solution strengthening effects in near-β titanium alloys. In addition, it is difficult to estimate β-size strengthening effects due to the complex variations in β morphology and distribution in Ti-64. Experimental studies of near-β alloys containing V and Al (Ti-10V-2Fe-3Al, Ti-5Al-5V-5Mo-3Cr and Ti-4.5Fe-7.2Cr-3Al) report yield stress values in the range 1000–1500 MPa [55–57]. Therefore, a friction stress of $\sigma_{\beta} = 1350$ MPa is assumed and fitted to Eq. (3). Combining Eqs. (1) and (3) describes the athermal contributions to the σ_Y

$$\sigma_Y = \left(\sigma_{\alpha} V_{\alpha} + \sigma_{\beta}(1 - V_{\alpha}) + \frac{k_{HP}}{\sqrt{D_{\alpha}}} \right) G(T, \dot{\varepsilon}) \qquad (9)$$

The thermally-activated processes are incorporated in Eq. (9) using a normalised activation energy G for dislocation cross-slip and it depends on the temperature (T) and strain rate ($\dot{\varepsilon}$). It can be described as follows [58,59]:

$$G = \left(\frac{\kappa \mu b^3}{k_B T ln\left(10^7 / \dot{\varepsilon} \right)} \right)^n \qquad (10)$$

with k_B is the Boltzmann constant and n and κ are constants adjusted to the experimental data reported in [4,32,34,38,60,61], giving values of 0.4 and 0.23, respectively. The shear modulus (μ) was determined as $\mu = (54 - 0.03\ T)$ GPa according to [58]. Finally, σ_Y can be predicted as a function of α volume fraction, mean α grain size, temperature and strain rate by substituting the Eq. (10) into Eq. (9).

3.2. Flow stress and strain hardening behaviour

The flow stress σ can be related to σ_Y and the dislocation evolution using the Taylor's equation [62], as follows:

$$\sigma = \sigma_Y + 0.3 M \mu b \sqrt{\rho} \qquad (11)$$

where M is the Taylor factor ranging from 0.05 to 3 for different materials, b is the Burgers vector and ρ is the average dislocation density of the material. The dislocation evolution is related to the competition between dislocation generation and annihilation with respect to the applied strain ε according to the Kocks-Mecking formulation [63], and can be described as follows:

$$\frac{d\rho}{d\varepsilon} = \frac{k_1}{b} \sqrt{\rho} - f\rho \qquad (12)$$

where k_1 is the dislocation generation coefficient and f is the recovery coefficient. By integrating and solving Eq. (12) the total dislocation density can be calculated as:

$$\rho = \left[\left(\frac{k_1}{bf} - \left(\frac{k_1}{bf} - \sqrt{\rho_0} \right) \right) e^{-\frac{1}{2}f\varepsilon} \right]^2 \qquad (13)$$

where ρ_0 is the initial dislocation density. Combining Eqs. (9), (10), (11) and (13), gives the expression of flow stress as follows:

$$\sigma = \left(\sigma_{\alpha} V_{\alpha} + \sigma_{\beta}(1 - V_{\alpha}) + \frac{k_{HP}}{\sqrt{D_{\alpha}}} \right) \left(\frac{\kappa \mu b^3}{k_b T ln\left(10^7 / \dot{\varepsilon} \right)} \right)^n$$
$$+ 0.3 M \mu b \left[\left(\frac{k_1}{bf} - \left(\frac{k_1}{bf} - \sqrt{\rho_0} \right) \right) e^{-\frac{1}{2}f\varepsilon} \right] \qquad (14)$$

It is worth to mention that for Ti-64 wrought, ρ_0 is usually considered to be very low, in the range 1×10^{11} m^{-2} [64], whereas, for martensitic structures its value has not been reported. Therefore, this parameter was estimated using the approach developed in [41].

The formation of martensite during rapid cooling is controlled by the transformation strain (ε_{trans}) of the transition from the β to α' phases [41]. The transformation strain is accommodated by dislocations and fine lamellar distributions forming in the as-quenched state. As a result, grain refinement and increased dislocation density, $\rho_{\alpha'}$, will promote an increase in the yield and flow stress (Eq. (14)). The dislocation density has been obtained for α' in steels by estimating the net strain energy accommodated by dislocations in a single martensite unit; $\rho_{\alpha'}$ was found to be proportional to ε_{trans} and the mean lamellar spacing $d_{\alpha'}$ [65] as:

$$\rho_{0\alpha'} = \frac{12 E w_{\alpha'}}{(1 + 2\nu^2)\mu b} \frac{\varepsilon_{trans}^2}{d_{\alpha'}^2} \qquad (15)$$

where $w_{\alpha'}$, is the α' lamellae thickness and $E = 110$ GPa is the Young's modulus of Ti-64. The transformation strain for Ti is reported to be $\varepsilon_{trans} = 0.1$ [41] and $w_{\alpha'} = 10$ nm is approximated from the work reported by Tarzimoghadam et al. [66]. Combining these results and considering an average lamellar spacing of 0.75 μm (Table 3) the initial dislocation density for the martensite phase can be given as $\rho_{0\alpha'} = 1.7 \times 10^{13}$ m^{-2}.

4. Results

This section presents the predicted values by the new model and its comparison with reported experimental data. Tables 2 and 3 present the physical constants used in this study and the microstructural features reported within the literature, respectively.

4.1. Yield strength of Ti-64

The predicted yield strength was validated for the materials and microstructural morphologies reported in Table 3. Fig. 4 shows the results compared with the experimentally measured values for AM processing routes (Fig. 4a) and three microstructures (Fig. 4b) including bimodal, lamellar and equiaxed structures. The dashed lines in Fig. 4 present the 5% error margin showing that the majority of the predicted results are within the ±5% error compared with the experimentally observed values reported in the literature.

Table 2
Constants parameters used for the model.

No.	Constant	Value	Units	Reference
1	k_{HP}	300	MPa	[67]
2	σ_{α}	550	MPa	Calculated
3	σ_{β}	1350	MPa	Calculated
4	M	3	–	Fitted
5	b	2.9×10^{-10}	m	[68]
6	k_B	1.38×10^{-23}	J/K	[68]
7	η	0.4	–	Fitted
8	κ	0.23	–	Fitted
9	f	8	–	Fitted
10	k_1	0.07	–	Fitted
12	ρ_0	1×10^{11}	m^{-2}	[64]
13	$\rho_{0\alpha'}$	1.7×10^{13}	m^{-2}	Calculated

Table 3
Microstructural features and deformation conditions tested in this work.

Author	Alpha average grain size D_α (μm)	Alpha lamella width W_α (μm)	Total volume fraction alpha V_α	Volume fraction lamellar alpha V_α	Volume fraction of equiaxed alpha (bimodal) V_α	Martensite average lath width $W_{\alpha'}$ (μm)	Volume fraction of martensite $V_{\alpha'}$	Microstructure type	Temperature (K)	Strain rate (s^{-1})
Park et al. [32]	9	0.6	0.72	0.28	0.85	–	–	Bimodal	298	10^{-3}–10
Park et al. [32]	13	–	0.85	–	–	–	–	Equiaxed	298	10^{-3}–10
Park et al. [32]	–	2.6	–	0.9	–	–	–	Lamellar	298	10^{-3}–10
Zheng et al. [34]	6	0.8	0.8	0.2	0.9	–	–	Bimodal	298	2600
Zheng et al. [34]	8	–	0.85	–	–	–	–	Equiaxed	298	2600
Zheng et al. [34]	9	2	–	0.9	–	–	–	Lamellar	298	2600
Khan et al. [16]	8	–	0.83	–	–	–	–	Equiaxed	298–755	10^{-6}–3378
Lee & Li [60]	8	–	0.9	–	–	–	–	Equiaxed	298–1373	2000
Li et al. [61]	–	–	–	–	–	0.75	1	PLD (α')	298–1273	0.1–5000
Kasperovich et al. [4]	5	–	0.83	–	–	–	–	Equiaxed	298	10^{-3}
Kasperovich et al. [4]	–	–	–	–	–	0.75	1	SLM (α')	298	10^{-3}
Kasperovich et al. [4]	1.5	–	0.98	–	–	–	–	SLM ($\alpha + \beta$)	298	10^{-3}
Kasperovich et al. [4]	2	–	0.97	–	–	–	–	SLM ($\alpha + \beta$)	298	10^{-3}
Kasperovich et al. [4]	3	–	0.95	–	–	–	–	SLM ($\alpha + \beta$)	298	10^{-3}

The model was validated against experimentally measured yield strengths under different deformation/microstructure conditions. Fig. 5.a shows the predicted yield strength for a martensitic structure produced by Powder Layer Deposition (PLD) technique at low and high strain rates (0.1 s^{-1} and 5000 s^{-1}) and temperatures ranging from 298 to 1273 K compared with the experimental results obtained from literature. Fig. 5.b presents the results of model validation for an equiaxed structure tested under different deformation conditions (5 strain rates and four temperatures). The dashed lines in Fig. 5 represent that the majority of the predicted results are within the ±5% error compared with the experimentally observed values reported in the literature.

These results suggest that the model can successfully predict the strength of martensitic structures such the ones generated through SLM and PLD technologies and can be easily used for C&W routes maintaining a maximum error of 5% in a wide range of deformation conditions.

4.2. Flow stress prediction

In order to validate the flow stress (σ) predictions, the effect of microstructural morphology on the flow stress of C&W structures (equiaxed, lamellar and bimodal) at low and high strain rates (1 $\times 10^{-2}$ up to 2600 s^{-1}) during room temperature was assessed. The model was then implemented for equiaxed and PLD (α') structures at an extensive range of deformation conditions. This is followed by final validation tests to compare the predicted flow stress for as-built SLM, SLM heat-treated and an equiaxed structures with the experimentally measured values reported in the literature.
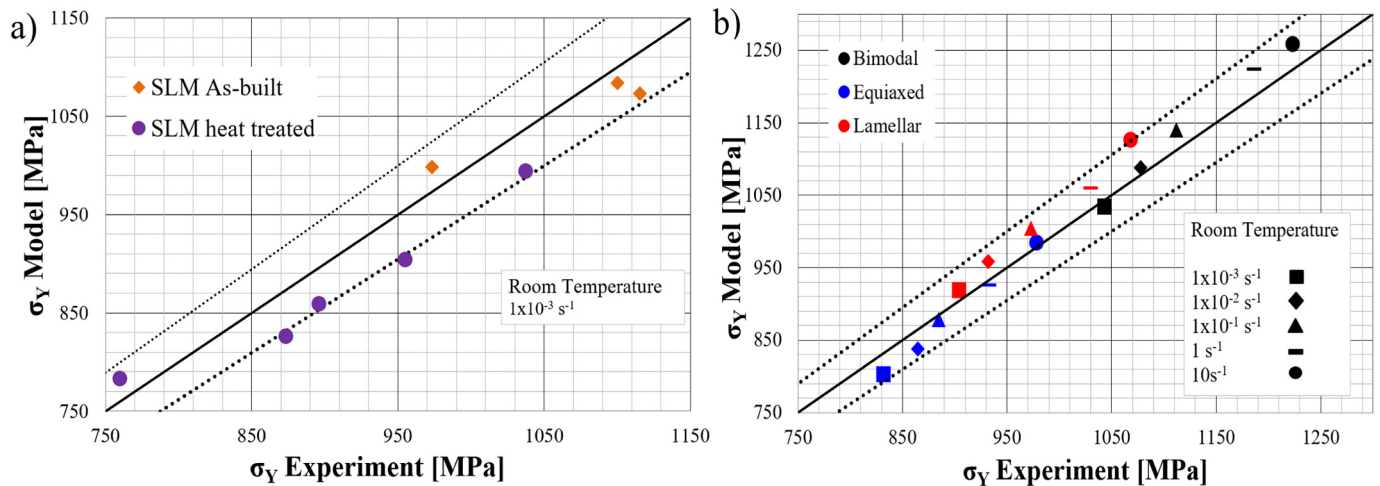

Fig. 4. Prediction of σ_Y for (a) SLM as-built, SLM heat treated [4] (b) hot worked structures at different strain rates [32]. All figures show σ_Y prediction (vertical axis) against the experimental results (horizontal axis) together with error margin of 5% (black dotted line).
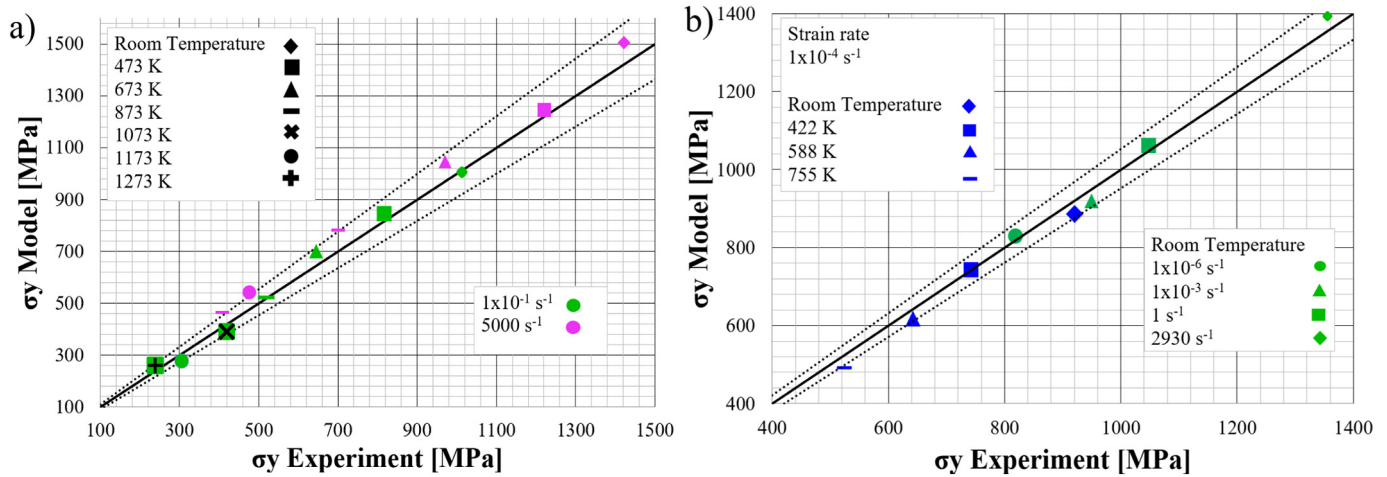
Fig. 5. Prediction of σ_Y for (a) PLD structures tested at various temperatures and under high and low speed testing condition [61], (b) equiaxed structure tested at various temperature and strain rates [16]. All figures show σ_Y prediction (vertical axis) against the experimental results (horizontal axis) together with error margin of 5% (black dotted line).

4.2.1. Cast and wrought microstructures

Fig. 6 shows the predicted plastic behaviour (solid lines) of hot worked structures (equiaxed, lamellar and bimodal) using low and high strain rates (1×10^{-2} up to 2600 s^{-1}) at the room temperature compared with the experimentally measured compression test results. The error bands show an error margin of 5% in the predicted results.
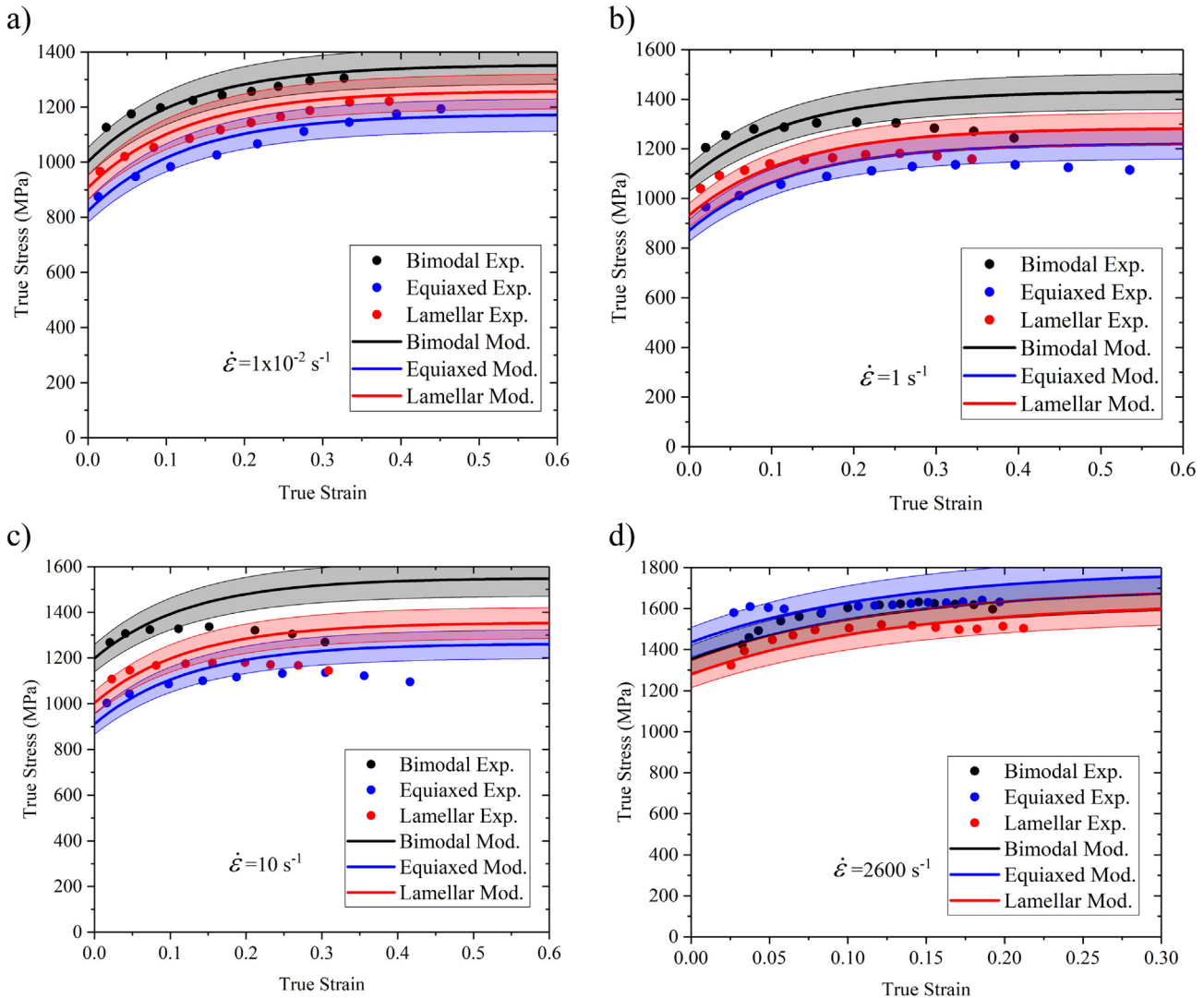
Fig. 6. Flow stress of hot worked Ti-64 structures [32,34], (a) 1×10^{-2} s^{-1}, (b) 1 s^{-1} (c) 10 s^{-1}, (d) 2600 s^{-1}, all at room temperature together with error margin of 5% (coloured error bands).

The predicted results show the least error (Fig. 6.a) for the lowest strain rate (1×10^{-2} s^{-1}) and the highest error (Fig. 6.c) for 10 s^{-1} strain rate. Whereas, strain rates within 1 s^{-1} and 2600 s^{-1} show intermediate results (Fig. 6.b and .d).

4.2.2. Equiaxed microstructures

The predicted flow stresses for an equiaxed microstructure under low (1×10^{-4} s^{-1}) and a high (2000 s^{-1}) deformation conditions are shown in Fig. 7a and b, respectively. The deformation temperature varied from 233 K up to 1373 K in both cases. According to the graphs of Fig. 7, the model predictions are closer to the experimental data at low strain rates. However, the model behaviour shows a deviation with the experimental data at the highest temperature tested (755 K) that can be related to the fact that the thermal softening prevails the strain rate hardening effect. In the deformation regime where the strain rate is much larger, this effect is less obvious therefore; the predicted results are closer to experiments even until a deformation temperature of 1173 K.

4.2.3. AM microstructures

Martensitic structures were verified from room temperature up to 1273 K and strain rates of 0.1 s^{-1} (Fig. 8.a) and 5000 s^{-1} (Fig. 8.b). Experimental data suggests that martensitic structures experience high strain hardening effect at low strain rates even at very high temperatures (1073–1273 K), whereas during a high strain rate deformation a thermal softening effect starts around 873 K.

Figs. 6 to 8 showed predicted results of two distinct processing routes (C&W and AM). However, it is common practice to post heat treat [4,36,46,47] and hot isostatic press (HIP) the AM components [4,46] in order to reduce the porosities and internal stresses within the produced parts [38]. Therefore, the model was validated during progression of AM microstructures (heat treated).

Fig. 9 shows stress-strain curves of SLM as-built (orange curve), SLM heat treated at 700 °C (red curve), 900 °C (grey curve) and HIP-ing at 900 °C (purple curve) and their corresponding microstructures [4]. The studied microstructural features are shown in Table 3. An equiaxed structure (green curve) with its mechanical response was added to compare C&W with SLM conditions. The schematics of the microstructures are presented to show their progress during post heat treatments and their mechanical response during tensile deformation.

The as-built SLM structure displays the highest strength compared to the post heat-treated (red, grey and purple curves) and equiaxed structures. The drop in strength is due to the coarsening of laths

(transition between orange to purple microstructures) as well as the decomposition of α' to $\alpha_s + \beta$ phases [4,69].

Together, the results show that the developed model was capable of predicting yield strength and hardening effect within the $\pm 5\%$ error compared with the experimental data of seven different Ti-64 microstructures (three C&W and four AM) in a wide range of deformation conditions.

5. Discussion

5.1. Yield strength predictions

According to Eq. (1), a remarkable increase in σ_Y is expected due to Ti-64 morphologies. For instance, bimodal microstructures possess the highest yield strength (Fig. 1.d) due to the increase of constitutive phases (α_p, α_s and β phases) by which the crystallographic misorientation increases, therefore greater impediment to dislocation movement. The lamellar structures exhibit a much finer α colony size than bimodal and equiaxed microstructures, hence, their yield strength increases due to greater total boundary area. Equiaxed structures present the lowest yield strength of the three microstructures due to the coarser α phase, whilst improving the ductility. Fig. 10 shows the variation of the σ_Y with respect to D_α of the V_α phase. The martensitic, lamellar and equiaxed microstructures are indicated by red, yellow and green regions, respectively. The size of α' laths ranging from 0.5 μm up to 1 μm leads to an increase in strength of about 400 MPa compared to equiaxed (8 μm) and lamellar (3 μm) structures, with a contribution of 100 ~MPa to ~170 MPa, respectively.

SLM as-built martensitic structures displayed higher strength compared to SLM heat-treated components that can be explained due to the martensite decomposition (change in constitutive phases) through $\alpha_s + \beta$ and subsequent grain growth as reported in [4,36,46]. This phenomenon has been verified through EBSD and XRD techniques exhibiting decomposition with an increase of beta phase (2–3%) and grain coarsening between 0.75 μm and 3 μm [40]. The post heat treatments in SLM components replicate the complex phase transformation that occurs during EBM process where the decomposition sequence of α' during EBM process is as follows; $\beta_{prior} \rightarrow \alpha' + \alpha_p + \beta_{retained} \rightarrow \alpha_s + \beta$ [69].

Table 4 shows the contribution of V_α and V_β in σ_Y for all the microstructures reported in Table 3. For predictions of SLM post heat-treated components, it is assumed that the materials are $\alpha + \beta$ with less than 5% of the β phase. Increasing V_β will promote friction stress
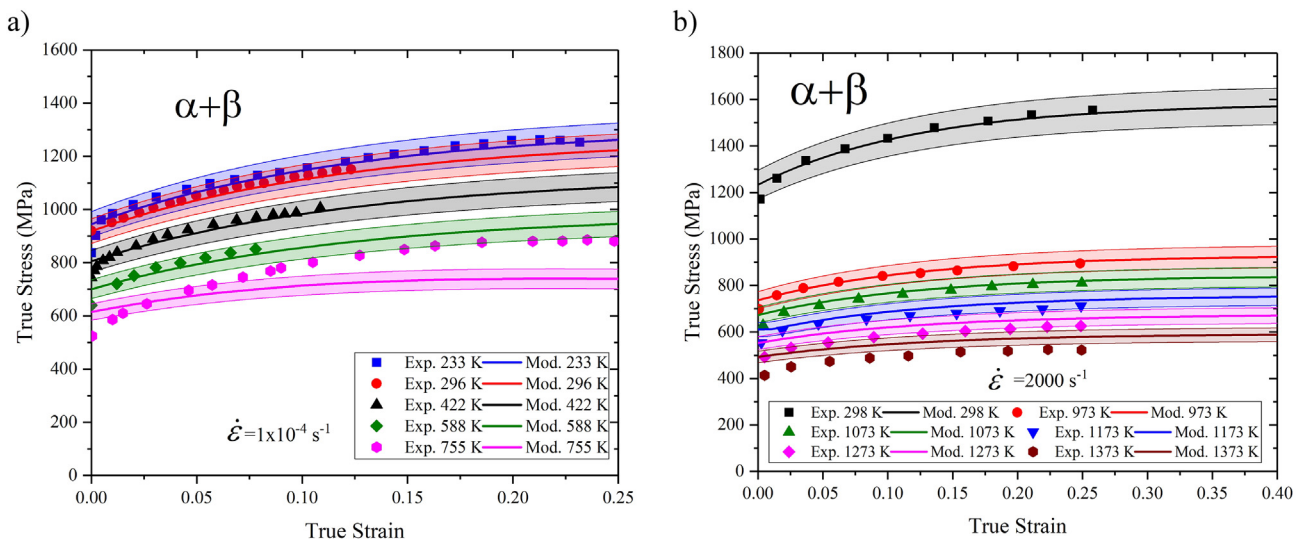

Fig. 7. Flow stress of equiaxed structures [16,24], (a) different temperatures and at 1×10^{-4} s^{-1} strain rate, (b) different temperatures and 2000 s^{-1} together with error margin of 5% (coloured error bands).
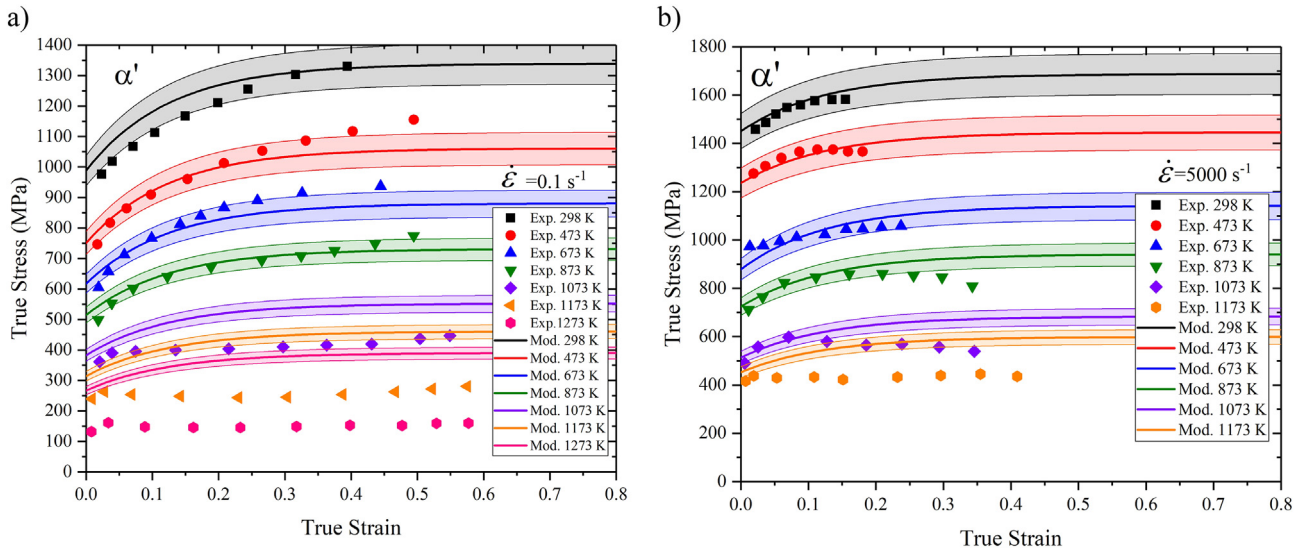
Fig. 8. Flow stress of martensitic structures [61] (a) 0.1 s^{-1} and (b) 5000 s^{-1} from room temperature up to 1273 K together with error margin of 5% in the coloured error bands.

of β (1350 MPa), whereas V_α contribution is just roughly one-third (544 MPa). Whereas for C&W, most of the as-received Ti-64 wrought alloys reported in the literature display V_α of about 80% up to 90% [4,9,16,32–34].

Moreover, results in Table 4 show that there is a competition between grain boundary and solid solution effects (relative volume fraction within the microstructure) as the model predicts σ_Y of 1034, 803 and 918 MPa for bimodal, equiaxed and lamellar, respectively. This is followed by quantifying the contribution of Hall-Petch (HP) = 355 MPa and σ_0 = 679 MPa for bimodal, HP = 94.5 MPa and σ_0 = 708.5 MPa for equiaxed and of HP = 209 MPa and σ_0 = 708 MPa for lamellar. Therefore, any changes in the microstructural morphology affect HP in a range between 94 MPa and 355 MPa while the variation of solid solution is within a smaller range (679–708.5 MPa).

5.2. Flow stress predictions

The flow stress predictions are sensitive to the dislocation generation coefficient, k_1, and dynamic recovery coefficient, f [63]. From Eq. (13) it can be seen that the evolution of dislocations is related to the dislocation generation and annihilation with respect to the applied strain ε. A benchmark equiaxed microstructure has been used to study the effect of these parameters on the flow stress wherein a yield strength of 882 MPa can be calculated for the material using the information given in Table 3. The graphs of Fig. 11 show the flow stress sensitivity in relation to the variations of k_1 and f. The experimental data and the predicted optimised flow curve are presented by the red and blue solid lines with square markers, respectively. The two parameters show to have an opposite effect on the predicted flow stress wherein at a fixed value of k_1 = 0.07, the larger f value results in smaller strain hardening and the flow stress saturates at a constant value of about 1100 MPa (Fig. 11.a). However, the variations of k_1 at a constant dynamic recovery coefficient results in a parabolic strain hardening behaviour together with a larger saturated flow stress (Fig. 11.b). Therefore, in order to calibrate the model, k_1 and f parameters were adjusted to the
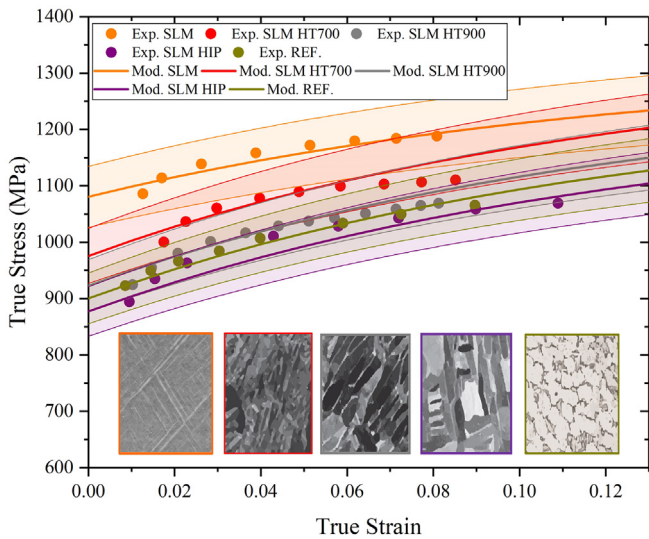

Fig. 9. Flow stress of Ti-64 structures; SLM as-built (orange) SLM heat treated at 700 C (red), 900 C (grey) and HIP-ing at 900 C (purple) equiaxed structure (green) all of them at a strain rate of 1×10^{-3} s^{-1}. Micrographs adapted from [4] together with error margin of 5% indicated by the error bands.
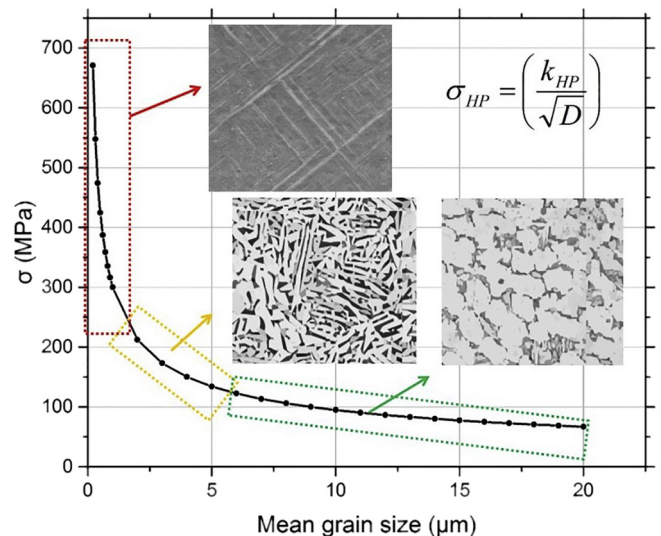

$$\sigma_{HP} = \left(\frac{k_{HP}}{\sqrt{D}}\right)$$

Fig. 10. Grain boundary strengthening in Ti-64's σ_Y.

Table 4
Solid solution contribution to σ_Y for diferent microstructures.

Author	Microstructure type	Volume fraction alpha V_α	Volume fraction lamellar alpha V_α	Volume fraction of equiaxed alpha (bimodal) V_α	Volume fraction of martensite $V_{\alpha'}$	Solid solution in α (MPa)	Solid solution in β (MPa)	Total solid solution contribution (MPa)
Park et al. [32]	Bimodal	0.72	0.28	0.85	–	392	378	679
Park et al. [32]	Equiaxed	0.9	–	–	–	490	135	708.5
Park et al. [32]	Lamellar	–	0.9	–	–	490	135	708
Zheng et al. [34]	Bimodal	0.8	0.2	0.9	–	435	270	705
Zheng et al. [34]	Equiaxed	0.85	–	–	–	462	203	665
Zheng et al. [34]	Lamellar	–	0.9	–	–	490	135	625
Khan et al. [16]	Equiaxed	0.83	–	–	–	452	230	681
Lee & Li [60]	Equiaxed	0.9	–	–	–	490	135	625
Li et al. [61]	PLD (α')	–	–	–	1	544	0	544
Kasperovich et al. [4]	Equiaxed	0.83	–	–	–	452	230	681
Kasperovich et al. [4]	SLM (α')	–	–	–	1	544	0	544
Kasperovich et al. [4]	SLM ($\alpha + \beta$)	0.98	–	–	–	533	27	560
Kasperovich et al. [4]	SLM ($\alpha + \beta$)	0.97	–	–	–	528	41	568
Kasperovich et al. [4]	SLM ($\alpha + \beta$)	0.95	–	–	–	517	68	584

experimental data reported in [4,32,34,38,60,61], giving values of 0.07 and 8, respectively.

Results from Fig. 6 show that at low strain rates (1×10^{-2} s^{-1}), a flow hardening effect is observed, while by increasing the strain rate (1–10 s^{-1}) the material displays the flow softening behaviour. This phenomenon could be caused by adiabatic shear bands generation, possibly, due to the presence of microstructural defects and inhomogeneities, rather than morphological effect during plastic deformation [32,70,71]. As the current model does not take such defects into account, the predicted flow curve deviates from the experimental data more than the proposed maximum error of 5%.

Another discrepancy in the modelling results was in the prediction of flow stress in equiaxed structures (Fig. 7) where experimental data shows that Ti-64 is more sensitive to temperature than the strain rate of deformation. The anisotropy of α phase could be responsible for results observed at temperature 755 K (Fig. 7.a). Ti-64, as part of the α + β family, has a high volume of α phase with a well-known HCP structure that is highly anisotropic [6,72]. Moreover, it is reported that in the C&W materials, the yield strength and the strain hardening are higher in compression than in tension [73,74]. In AM build Ti-64, it is well recognised that the build direction highly affects the mechanical properties (yield strength and ductility) [47,75]. The proposed model is not taking into account the anisotropic behaviour of the materials, and assumes that all the studied materials are homogeneous and isotropic. However the anisotropy effect can be implemented through Taylor's orientation factor M in Eq. (11) [62]. The effects of individual grains orientation, within the cross-section of a specimen, on the flow stress can also be calculated as reported in [76].

Although the model is capable to closely follow the experimental data up to 1173 K (Fig. 7.b), the predictions are not accurate beyond this temperature. There are several studies investigating the behaviour of Ti-64 during hot deformation [33,77] reporting dynamic
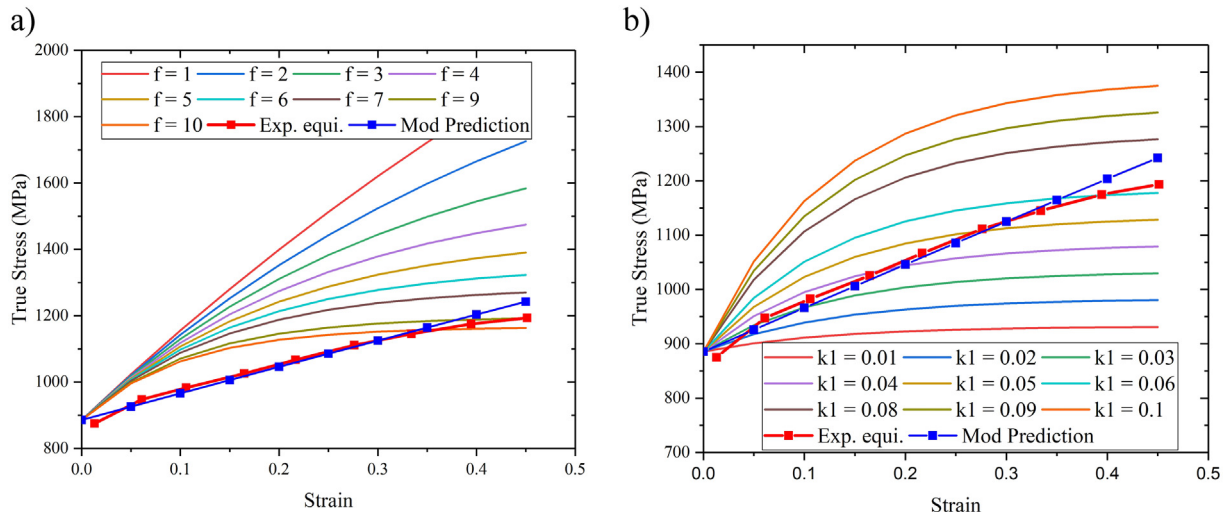

Fig. 11. (a) Effect of f and (b) k_1 parameters into flow stress of an equiaxed structure with a 13 μm mean grain size and $V_\alpha = 0.85$ during room temperature and strain rate of 1×10^{-2} s^{-1}.

globularization phenomenon that creates a peak stress followed by softening during certain strain and range of temperature [7,33,77]. However, this mechanism lies beyond the scope of the present work.

The model predictions of hot deformation in martensitic structures (Fig. 8) are reasonably accurate up to 873 K for both strain rates. However from 1073 K, the experimental results display a drastic drop in strength (from 0.1 s^{-1} = ~150 MPa and 5000 s^{-1} = ~200 MPa). This softening effect could be due to α' decomposition which is at about 873 K, as reported in [4,47,78], displaying a change in the grain size also in the constitutive phases.

The discrepancies can be explained due to the fact that C&W Ti-64 experiences a phase transformation at 1173 K, whereas for the AM structure, the martensite start temperature (M$_s$) depends on the aluminium and oxygen levels, but for pure titanium lies around 1123 K [37]. Thus a progression in the microstructure is expected in both alloys despite the manufacturing method. As a result, the initial microstructural features reported in Table 3 defer during high temperatures. In addition, the role that β phase plays during hot deformation is not clearly understood [7]. Therefore, further research is being prepared by the authors to study these mechanisms in more detail.

Last validation (Fig. 9) consisted in transition between martensitic structures (as-built SLM) through evolved structures (SLM post heat-treated). The results showed good agreement with the predicted flow curves. As mentioned previously in Section 5.1, SLM post heat-treated achieve similar structures as the ones achieved by EBM techniques (no martensite present). This can be explained because of the differences between SLM and EBM processes. During EBM, the substrate (building bed) is heated at high temperatures (roughly 873 K) [36] due to the action of the heat source (electron beam); hence the cooling rate remains low enough to decompose α'. In contrast, during SLM process the substrate is heated at ~373 K, therefore much higher cooling rates are inherit in the process, hence α' is formed. The results in Fig. 9 also indicate that the model could be extended to predict the microstructures obtained by EBM technologies and aid to optimise the heat treatments [7,78].

AM technologies currently are taking advantage of the well stablished wrought alloy compositions through pre-alloyed powder, but not much effort has been paid on designing alloys for specific AM technologies. Hence, next section presents hypothetical examples varying chemical composition and fixing microstructural features.

5.3. Case study: design of Ti-based alloys using the developed model

Since the model is sensitive to variations in chemical composition, via changing the relative volume fraction of α and β and the solid solution strengthening terms, it is interesting to explore the role of Al and V in the overall strengthening of Ti-64. The Thermodynamic software Thermocalc, with the TTTi3 database, was used to predict the volume fraction of α and β in equilibrium; the calculations were performed at 1073 K, as it is a common temperature employed annealing this alloy [37]. Table 5 presents the results of the hypothetical study varying Al and V separately (2–8 wt%) wherein the results show that the strength of Ti-alloys is highly affected by V_α. Additionally, it presents the

contribution of solid solution within alpha and beta phases respectively and the total contribution to yield strength.

It is worth to mention that the morphology and the relative volume fraction of alpha are entirely dependent of the thermo-mechanical processing route before and after annealing step [6]. However, in order to predict yield strength, for this study, an equiaxed structure of 15 μm mean grain size was considered. Fig. 12 shows the combined effect of varying Al or V against the yield strength. The 6Al-8V alloy (V_α = 0.53) showed the highest strength, whereas 6Al-2V alloy (V_α = 1) obtained the lowest strength within all the tested alloys. It is well known that near-α alloys present the lowest strength and the near-β alloys the highest strength within the Ti-family. The alloys Ti-2Al-4V and Ti-6Al-8V display comparable yield strength (1134 MPa and 1171 MPa, respectively). Similar results are achieved with Ti-8Al-4V and Ti-6Al-2V predicting 793 MPa and 730 MPa, respectively. This can be explained due to the presence of analogous V_α between the four alloys predicted by Thermo-calc through 1073 K annealing temperature.

The new proposed model could be used for rationalising variations in mechanical properties targeted at alloy development, either under conventional C&W or AM processing conditions. The wrought $\alpha + \beta$ alloys popularity lies in two factors; their response to heat treatments and good formability [6], as result, $\alpha + \beta$ alloys possess wider processing window compared to near-α and near-β alloys. Therefore, process optimisation has been a challenging topic in the C&W field, whereas for AM technology is currently focused in two main areas of development of new alloys [45,79] and to aid to manufacture difficult-to process Ti-alloys such as the well-known Ti-5553 alloy [80–82].

These results provide important insights into current optimisation of microstructures produced by C&W and also those obtained by AM and their post heat treatments. Additionally, it is capable to quantify the strengthening mechanisms affecting Ti-alloys strength via linking relevant microstructural features, therefore the model could be used as a tool for new AM generation alloys.

6. Conclusions

The following conclusions can be drawn from this work:

• A new physically-based model that describes strength and flow stress of additively manufactured and Cast-and-wrought Ti-64 has been introduced. The research has also shown that the new model can be extended to other Ti-alloys.
• A transition from microstructures obtained by AM (martensitic) and C&W (equiaxed and lamellar $\alpha + \beta$) was achieved through
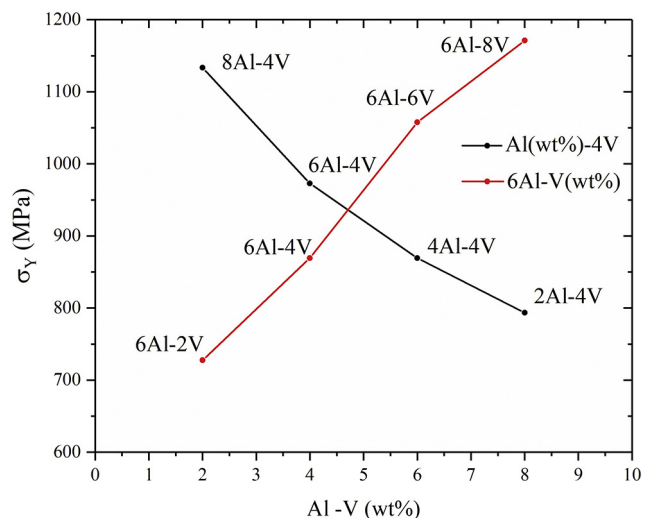
Table 5
Solid solution contribution using Thermocalc results of V_α at 1073 K annealing temperature.

Al (wt%)	V (wt%)	V_α	σ_α (MPa)	σ_β (MPa)	σ_{ss} (MPa)
2	4	0.57	310.08	580.5	890.58
4	4	0.74	402.56	351	753.56
6	4	0.85	462.4	202.5	664.9
8	4	0.93	505.92	94.5	600.42
6	2	1	544	0	544
6	6	0.65	353.6	472.5	826.1
6	8	0.53	288.32	634.5	922.82

Fig. 12. Chemical composition effect into σ_Y of Ti-alloys with a 15 μm mean grain size, during room temperature and strain rate of 1×10^{-2} s^{-1}.

quantification of constitutive phases and morphology. Seven microstructures were tested, three for C&W and four under AM, in a wide range of deformation conditions: strain rates as low as $0.001\,\mathrm{s}^{-1}$ and as high as $5000\,\mathrm{s}^{-1}$ and temperatures ranging from room temperature up to 1373 K.

- It was shown that the strength of Ti-64 is mostly affected by the relative fraction of α, β and α', and their respective morphology (which is reflected by grain boundary strengthening). Analogous to α' in steels, it was shown that martensite provides the strength in titanium alloys by grain refinement and an increase of dislocation density during rapid cooling.

- For the case of hot deformation (1173 K and higher temperatures) the model had difficulties to predict the values, this discrepancy was attributed to microstructure progression, hence the initial microstructure parameters defer during high temperatures. Further research is being prepared by the authors to study in more detail these conditions.

Authors contributions

Marco Galindo wrote the 1st draft of the paper and run simulations.

K. Mumtaz helped with his expertise in additive manufacturing of metals to produce the requires samples and brought the expertise related to AM technologies. Dr. Mumtaz also reviewed the final draft of the paper.

P. Rivera helped to develop equations for the model and validation of it.

E. Galindo worked closely with Mr. Marco Galindo to the model develop and highly contributed to the model.

Dr. H. Ghadbeigi, as the primary PhD supervisor of Mr. Marco Galindo, is the main responsible of the conducted research and rewrote most of the paper according to the initial input and obtained experimental results. He is also contributed heavily on the revision of the paper and provision of responses to the reviewers' comments. Dr. Ghadbeigi provided the expertise and required funding to conduct the experimental work and analysis of the results obtained by Mr. Marco Galindo.

Acknowledgments

References

[1] L. Guo, X. Fan, G. Yu, H. Yang, Microstructure control techniques in primary hot working of titanium alloy bars: a review, Chin. J. Aeronaut. 29 (2016) 30–40 (2016/02/01/).

[2] G. Chen, C. Ren, X. Qin, J. Li, Temperature dependent work hardening in Ti–6Al–4V alloy over large temperature and strain rate ranges: experiments and constitutive modeling, Mater. Des. 83 (2015) 598–610 (2015/10/15/).

[3] X. Zhao, S. Li, M. Zhang, Y. Liu, T.B. Sercombe, S. Wang, et al., Comparison of the microstructures and mechanical properties of Ti–6Al–4V fabricated by selective laser melting and electron beam melting, Mater. Des. 95 (2016) 21–31 (2016/04/05/).

[4] G. Kasperovich, J. Hausmann, Improvement of fatigue resistance and ductility of TiAl6V4 processed by selective laser melting, J. Mater. Process. Technol. 220 (2015) 202–214 (6//).

[5] P. Li, D.H. Warner, A. Fatemi, N. Phan, Critical assessment of the fatigue performance of additively manufactured Ti–6Al–4V and perspective for future research, Int. J. Fatigue 85 (2016) 130–143 (4//).

[6] G. Lütjering, Influence of processing on microstructure and mechanical properties of $(\alpha + \beta)$ titanium alloys, Mater. Sci. Eng. A 243 (1998) 32–45 (3/15/).

[7] Z.X. Zhang, S.J. Qu, A.H. Feng, J. Shen, D.L. Chen, Hot deformation behavior of Ti–6Al–4V alloy: Effect of initial microstructure, J. Alloys Compd. 718 (2017) 170–181 (2017/09/25/).

[8] D.D. Gu, W. Meiners, K. Wissenbach, R. Poprawe, Laser additive manufacturing of metallic components: materials, processes and mechanisms, Int. Mater. Rev. 57 (2012) 133–164 (2012/05/01).

[9] S. Nemat-Nasser, W.-G. Guo, V.F. Nesterenko, S.S. Indrakanti, Y.-B. Gu, Dynamic response of conventional and hot isostatically pressed Ti–6Al–4V alloys: experiments and modeling, Mech. Mater. 33 (2001) 425–439 (2001/08/01/).

[10] C. Zhang, X.-q. Li, D.-s. Li, C.-h. Jin, J.-j. Xiao, Modelization and comparison of Norton-Hoff and Arrhenius constitutive laws to predict hot tensile behavior of Ti–6Al–4V alloy, Trans. Nonferrous Metals Soc. China 22 (2012) s457–s464 (2012/12/01/).

[11] M.A. Shafaat, H. Omidvar, B. Fallah, Prediction of hot compression flow curves of Ti–6Al–4V alloy in $\alpha + \beta$ phase region, Mater. Des. 32 (2011) 4689–4695 (2011/12/01/).

[12] B. Babu, L.-E. Lindgren, Dislocation density based model for plastic deformation and globularization of Ti–6Al–4V, Int. J. Plast. 50 (2013) 94–108 (2013/11/01/).

[13] J. G. R. C. W.H, A constitutive model and data for metals subjected to large strains, high strain rates and high temperatures, Proceedings of the 7th International Symposium on Ballistics 1983, pp. 1816–1825.

[14] S. Seo, O. Min, H. Yang, Constitutive equation for Ti–6Al–4V at high temperatures measured using the SHPB technique, Int. J. Impact Eng. 31 (2005) 735–754 (7//).

[15] A.S. Khan, R. Liang, Behaviors of three BCC metal over a wide range of strain rates and temperatures: experiments and modeling, Int. J. Plast. 15 (1999) 1089–1109 (1999/01/01/).

[16] A.S. Khan, Y. Sung Suh, R. Kazmi, Quasi-static and dynamic loading responses and constitutive modeling of titanium alloys, Int. J. Plast. 20 (2004) 2233–2248 (12//).

[17] U.F. Kocks, H. Mecking, Physics and phenomenology of strain hardening: the FCC case, Prog. Mater. Sci. 48 (2003) 171–273.

[18] Y. Bergström, The plastic deformation of metals - a dislocation model and its applicability, Rev. Powder Metall. Phys. Ceram. 2 (1983) 79–265.

[19] A. Tabei, F.H. Abed, G.Z. Voyiadjis, H. Garmestani, Constitutive modeling of Ti–6Al–4V at a wide range of temperatures and strain rates, Eur. J. Mech. A. Solids 63 (2017) 128–135 (2017/05/01/).

[20] S. Anurag, Y.B. Guo, A modified micromechanical approach to determine flow stress of work materials experiencing complex deformation histories in manufacturing processes, Int. J. Mech. Sci. 49 (2007) 909–918 (2007/09/01/).

[21] J. Xiao, D.S. Li, X.Q. Li, T.S. Deng, Constitutive modeling and microstructure change of Ti–6Al–4V during the hot tensile deformation, J. Alloys Compd. 541 (2012) 346–352 (2012/11/15/).

[22] Y. Sun, W. Zeng, Y. Han, Y. Zhao, G. Wang, M.S. Dargusch, et al., Modeling the correlation between microstructure and the properties of the Ti–6Al–4V alloy based on an artificial neural network, Mater. Sci. Eng. A 528 (2011) 8757–8764 (2011/11/15/).

[23] W. Yu, M.Q. Li, J. Luo, S. Su, C. Li, Prediction of the mechanical properties of the post-forged Ti–6Al–4V alloy using fuzzy neural network, Mater. Des. 31 (2010) 3282–3288 (2010/08/01/).

[24] W.-S. Lee, C.-F. Lin, High-temperature deformation behaviour of Ti6Al4V alloy evaluated by high strain-rate compression tests, J. Mater. Process. Technol. 75 (1998) 127–136 (3/1/).

[25] N. Kotkunde, A.D. Deole, A.K. Gupta, S.K. Singh, Comparative study of constitutive modeling for Ti–6Al–4V alloy at low strain rates and elevated temperatures, Mater. Des. 55 (2014) 999–1005 (2014/03/01/).

[26] H.W. Meyer, D.S. Kleponis, Modeling the high strain rate behavior of titanium undergoing ballistic impact and penetration, Int. J. Impact Eng. 26 (2001) 509–521 (2001/12/01).

[27] M. Sima, T. Özel, Modified material constitutive models for serrated chip formation simulations and experimental validation in machining of titanium alloy Ti–6Al–4V, Int. J. Mach. Tools Manuf. 50 (2010) 943–960 (11//).

[28] H. Mecking, Y. Estrin, The effect of vacancy generation on plastic deformation, Scr. Metall. 14 (1980) 815–819 (1980/07/01/).

[29] C. Baykasoglu, O. Akyildiz, D. Candemir, Q. Yang, A.C. To, Predicting microstructure evolution during directed energy deposition additive manufacturing of Ti-6Al-4V, J. Manuf. Sci. Eng. 140 (2018) pp. 051003-051003-11.

[30] Effect of phase transformations on laser forming of Ti–6Al–4V alloy, J. Appl. Phys. 98 (2005), 013518. .

[31] B.J. Hayes, B.W. Martin, B. Welk, S.J. Kuhr, T.K. Ales, D.A. Brice, et al., Predicting tensile properties of Ti-6Al-4V produced via directed energy deposition, Acta Mater. 133 (2017) 120–133 (2017/07/01/).

[32] C.H. Park, Y.I. Son, C.S. Lee, Constitutive analysis of compressive deformation behavior of ELI-grade Ti–6Al–4V with different microstructures, J. Mater. Sci. 47 (2012) 3115–3124.

[33] S.L. Semiatin, T.R. Bieler, The effect of alpha platelet thickness on plastic flow during hot working of TI–6Al–4V with a transformed microstructure, Acta Mater. 49 (2001) 3565–3573 (2001/10/09/).

[34] C. Zheng, F. Wang, X. Cheng, K. Fu, J. Liu, Y. Wang, et al., Effect of microstructures on ballistic impact property of Ti–6Al–4V targets, Mater. Sci. Eng. A 608 (2014) 53–62 (7/1/).

[35] W. Xu, S. Sun, J. Elambasseril, Q. Liu, M. Brandt, M. Qian, Ti-6Al-4V additively manufactured by selective laser melting with superior mechanical properties, JOM 67 (2015) 668–673.

[36] L. Facchini, E. Magalini, P. Robotti, A. Molinari, S. Höges, K. Wissenbach, Ductility of a Ti-6Al-4V alloy produced by selective laser melting of prealloyed powders, Rapid Prototyp. J. 16 (2010) 450–459.

[37] J.C. Williams, G. Lütjering, Titanium, Springer, Berlin, 2003.

[38] H. Gong, K. Rafi, H. Gu, G.D. Janaki Ram, T. Starr, B. Stucker, Influence of defects on mechanical properties of Ti–6Al–4 V components produced by selective laser melting and electron beam melting, Mater. Des. 86 (2015) 545–554 (12/5/).

[39] W. Xu, M. Brandt, S. Sun, J. Elambasseril, Q. Liu, K. Latham, et al., Additive manufacturing of strong and ductile Ti–6Al–4V by selective laser melting via in situ martensite decomposition, Acta Mater. 85 (2015) 74–84 (2/15/).

[40] S. Leuders, M. Thöne, A. Riemer, T. Niendorf, T. Tröster, H.A. Richard, et al., On the mechanical behaviour of titanium alloy TiAl6V4 manufactured by selective laser melting: Fatigue resistance and crack growth performance, Int. J. Fatigue 48 (2013) 300–307 (3//).

[41] E.I. Galindo-Nava, On the prediction of martensite formation in metals, Scr. Mater. 138 (2017) 6–11 (2017/09/01/).

[42] I. Yadroitsev, P. Krakhmalev, I. Yadroitsava, Selective laser melting of Ti6Al4V alloy for biomedical applications: temperature monitoring and microstructural evolution, J. Alloys Compd. 583 (2014) 404–409 (2014/01/15/).

[43] P. Edwards, M. Ramulu, Fatigue performance evaluation of selective laser melted Ti–6Al–4V, Mater. Sci. Eng. A 598 (2014) 327–337 (3/26/).

[44] H.K. Rafi, T.L. Starr, B.E. Stucker, A comparison of the tensile, fatigue, and fracture behavior of Ti–6Al–4V and 15-5 PH stainless steel parts made by selective laser melting, Int. J. Adv. Manuf. Technol. 69 (2013) 1299–1309.

[45] E.O. Hall, The deformation and ageing of mild steel: III discussion of results, Proc. Phys. Soc. London, Sect. B 64 (1951) 747.

[46] H.W. Rosenberg, W.D. Nix, Solid solution strengthening in Ti-Al alloys, Metall. Trans. 4 (May 01 1973) 1333–1338.

[47] A. Akhtar, E. Teghtsoonian, Prismatic slip in α-titanium single crystals, Metall. Mater. Trans. A 6 (December 01 1975) 2201.

[48] R. Labusch, A statistical theory of solid solution hardening, Phys. Status Solidi B 41 (1970) 659–669.

[49] E.I. Galindo-Nava, L.D. Connor, C.M.F. Rae, On the prediction of the yield stress of unimodal and multimodal γ′ Nickel-base superalloys, Acta Mater. 98 (2015) 377–390 (2015/10/01/).

[50] D.R. Lide, CRC handbook of chemistry and physics, J. Mol. Struct. 268 (1992) 320 (1992/04/01/).

[51] D.N. Williams, R.A. Wood, R.I. Jaffee, H.R. Ogden, The effects of zirconium in titanium-base alloys, J. Less-Common Met. 6 (1964) 219–225 (1964/03/01/).

[52] T. Duerig, J. Williams, Overview: microstructure and properties of beta titanium alloys, Beta Titanium Alloys in the 1980's 1983, pp. 19–67.

[53] B.A. Welk, Microstructural and property relationships in β-titanium alloy Ti-5553 (PhD dissertation, The Ohio State University, 2010), Master's Materials Science and Engineering, The Ohio State University, Ohio, 2010.

[54] P.E. Markovsky, M. Ikeda, Balancing of mechanical properties of Ti–4.5 Fe–7.2Cr–3.0 Al using thermomechanical processing and rapid heat treatment, Mater. Trans. 46 (2005) 1515–1524.

[55] E.I. Galindo-Nava, P.E.J. Rivera-Díaz-del-Castillo, A thermostatistical theory of low and high temperature deformation in metals, Mater. Sci. Eng. A 543 (2012) 110–116 (5/1/).

[56] P.S. Follansbee, G.T. Gray, An analysis of the low temperature, low and high strain-rate deformation of Ti−6Al−4V, Metall. Trans. A. 20 (1989) 863–874.

[57] W.-S. Lee, C.-F. Lin, Plastic deformation and fracture behaviour of Ti–6Al–4V alloy loaded with high strain rate under various temperatures, Mater. Sci. Eng. A 241 (1998) 48–59 (1//).

[58] P.-H. Li, W.-G. Guo, W.-D. Huang, Y. Su, X. Lin, K.-B. Yuan, Thermomechanical response of 3D laser-deposited Ti–6Al–4V alloy over a wide range of strain rates and temperatures, Mater. Sci. Eng. A 647 (2015) 34–42 (10/28/).

[59] The mechanism of plastic deformation of crystals. Part II.—comparison with observations, Proc. R. Soc. London, Ser. A 145 (1934) 388–404.

[60] U.F. Kocks, Laws for work-hardening and low-temperature creep, J. Eng. Mater. Technol. 98 (1976) 76–85.

[61] E.I. Galindo-Nava, C.M.F. Rae, Microstructure-sensitive modelling of dislocation creep in polycrystalline FCC alloys: Orowan theory revisited, Mater. Sci. Eng. A 651 (2016) 116–126 (2016/01/10/).

[62] E.I. Galindo-Nava, P.E.J. Rivera-Díaz-del-Castillo, A model for the microstructure behaviour and strength evolution in lath martensite, Acta Mater. 98 (2015) 81–93 (2015/10/01/).

[63] Z. Tarzimoghadam, S. Sandlöbes, K.G. Pradeep, D. Raabe, Microstructure design and mechanical properties in a near-α Ti–4Mo alloy, Acta Mater. 97 (2015) 291–304 (2015/09/15/).

[64] C.-Y. Hyun, H.-K. Kim, The comparison of yield and fatigue strength dependence on grain size of pure Ti produced by severe plastic deformation, Rev. Adv. Mater. Sci. 28 (2011) 69–73.

[65] H.J. Frost, M.F. Ashby, Deformation Mechanism Maps: The Plasticity and Creep of Metals and Ceramics, Pergamon press, 1982.

[66] T. Vilaro, C. Colin, J.D. Bartout, As-fabricated and heat-treated microstructures of the Ti-6Al-4V alloy processed by selective laser melting, Metall. Mater. Trans. A 42 (2011) 3190–3199.

[67] K. Rekedal, Investigation of the high-cycle fatigue life of selective laser melted and hot isostatically presses Ti-6Al-4V, PhD dissertation, air force institute of technology, Air University, Ohio, 2015.

[68] X. Tan, Y. Kok, W.Q. Toh, Y.J. Tan, M. Descoins, D. Mangelinck, et al., Revealing martensitic transformation and α/β interface evolution in electron beam melting three-dimensional-printed Ti-6Al-4V, 6 (2016) 26039 (05/17/online).

[69] A.J.W. Johnson, K.S. Kumar, C.L. Briant, Strengthening mechanisms in Ti-6Al-4V/TiC composites, AIP Conf. Proc. 712 (2004) 1639–1644.

[70] D.-G. Lee, S. Lee, C.S. Lee, S. Hur, Effects of microstructural factors on quasi-static and dynamic deformation behaviors of Ti-6Al-4V alloys with widmanstätten structures, Metall. Mater. Trans. A 34 (November 01 2003) 2541.

[71] E.I. Galindo-Nava, Modelling twinning evolution during plastic deformation in hexagonal close-packed metals, Mater. Des. 83 (2015) 327–343 (2015/10/15/).

[72] V. Tuninetti, A.M. Habraken, Impact of anisotropy and viscosity to model the mechanical behavior of Ti–6Al–4V alloy, Mater. Sci. Eng. A 605 (2014) 39–50 (2014/05/27/).

[73] V. Tuninetti, G. Gilles, O. Milis, T. Pardoen, A.M. Habraken, Anisotropy and tension–compression asymmetry modeling of the room temperature plastic response of Ti–6Al–4V, Int. J. Plast. 67 (2015) 53–68 (2015/04/01/).

[74] L.Y. Chen, J.C. Huang, C.H. Lin, C.T. Pan, S.Y. Chen, T.L. Yang, et al., Anisotropic response of Ti-6Al-4V alloy fabricated by 3D printing selective laser melting, Mater. Sci. Eng. A 682 (2017) 389–395 (2017/01/13/).

[75] H. Justinger, G. Hirt, Estimation of grain size and grain orientation influence in microforming processes by Taylor factor considerations, J. Mater. Process. Technol. 209 (2009) 2111–2121 (2009/02/19/).

[76] S.L. Semiatin, V. Seetharaman, I. Weiss, Flow behavior and globularization kinetics during hot working of Ti–6Al–4V with a colony alpha microstructure, Mater. Sci. Eng. A 263 (1999) 257–271 (5/15/).

[77] H. Ali, L. Ma, H. Ghadbeigi, K. Mumtaz, In-situ residual stress reduction, martensitic decomposition and mechanical properties enhancement through high temperature powder bed pre-heating of Selective Laser Melted Ti6Al4V, Mater. Sci. Eng. A 695 (2017) 211–220 (2017/05/17/).

[78] L.-C. Zhang, H. Attar, Selective laser melting of titanium alloys and titanium matrix composites for biomedical applications: a review, Adv. Eng. Mater. 18 (2016) 463–475.

[79] B. Vrancken, L. Thijs, J.P. Kruth, J. Van Humbeeck, Microstructure and mechanical properties of a novel β titanium metallic composite by selective laser melting, Acta Mater. 68 (2014) 150–158 (4/15/).

[80] H. Schwab, F. Palm, U. Kühn, J. Eckert, Microstructure and mechanical properties of the near-beta titanium alloy Ti-5553 processed by selective laser melting, Mater. Des. 105 (2016) 75–80 (2016/09/05/).

[81] C. Zopp, S. Blümer, F. Schubert, L. Kroll, Processing of a metastable titanium alloy (Ti-5553) by selective laser melting, Ain Shams Eng. J. 8 (2017) 475–479 (2017/09/01/).

[82] H. Schwab, M. Bönisch, L. Giebeler, T. Gustmann, J. Eckert, U. Kühn, Processing of Ti-5553 with improved mechanical properties via an in-situ heat treatment combining selective laser melting and substrate plate heating, Mater. Des. 130 (2017) 83–89 (2017/09/15/).